Journal of Materials Chemistry C

ROYAL SOCIETY OF CHEMISTRY

PAPER

View Article Online
View Journal

Cite this: DOI: 10.1039/d6tc00262e

Influence of composition and structure on resistive switching properties of hafnium–titanium-oxide thin films grown by atomic layer deposition

Toomas Daniel Viskus, *[a] Lauri Aarik, [a] Tõnis Arroval,[a] Aarne Kasikov, [a] Joonas Merisalu, [a] Jekaterina Kozlova, [a] Markus Otsus, [a] Hugo Mändar,[a] Jaan Aarik, [a] Guillermo Vinuesa, [b] Salvador Dueñas, [b] Helena Castán [b] and Kaupo Kukli [a]

Resistive switching devices based on $Hf_xTi_{1-x}O_y$ thin films with Hf/(Hf + Ti) cation ratios (x) of 0.07–0.64 were studied. The $Hf_xTi_{1-x}O_y$ films were grown by atomic layer deposition (ALD) using $TiCl_4$, $HfCl_4$ and H_2O as precursors in supercycles that included different numbers of TiO_2 ALD cycles and a single HfO_2 ALD cycle. The films were grown onto RuO_2 bottom electrodes at 350 °C. Pt top electrodes were deposited by electron beam evaporation. The $Hf_xTi_{1-x}O_y$ films with the x values 0.07–0.19 predominantly contained the rutile phase, while a crystalline phase isomorphous with the orthorhombic $HfTiO_4$ was formed in the films with x of 0.30–0.64. The elemental and phase compositions had a marked effect on electrical characteristics of the films. Significant increase in the breakdown electric field strength (E_B) was observed when x increased from 0.07 to 0.19 resulting in E_B values of 4.7–6.3 MV cm^{-1} for $Hf_xTi_{1-x}O_y$ with x ranging from 0.19 to 0.64. Most importantly, the samples containing the orthorhombic phase demonstrated superior resistive switching performance, that is, low-resistive-state (LRS) to high-resistive-state (HRS) conductance ratios >100 and endurance exceeding 10^4 resistive switching cycles at room temperature, excellent retention of LRS and HRS at 110 °C, and resistive switching at temperatures up to 140 °C. Measurements with various pulse widths of the applied voltage revealed that the reset process limited the operation speed of these devices.

Received 26th January 2026,
Accepted 6th May 2026

DOI: 10.1039/d6tc00262e

rsc.li/materials-c

1. Introduction

Materials exhibiting resistive switching (RS) phenomena have been investigated thoroughly for applications in a type of non-volatile memory typically referred to as resistive random-access memory (RRAM).[1–3] Fundamentally, the RS effect relies on the non-volatile and reversible modification of a device (typically a metal–insulator–metal stack) resistance when applying an electrical stimulus. This mechanism requires an initial electroforming step to create a conductive filament (CF) across the insulating layer for the first time. After this, the device can be repeatedly switched between a high-resistive state (HRS) and a low-resistive state (LRS) by rupturing the CF during the reset process and re-forming it during the set process, respectively (Fig. 1).[4]

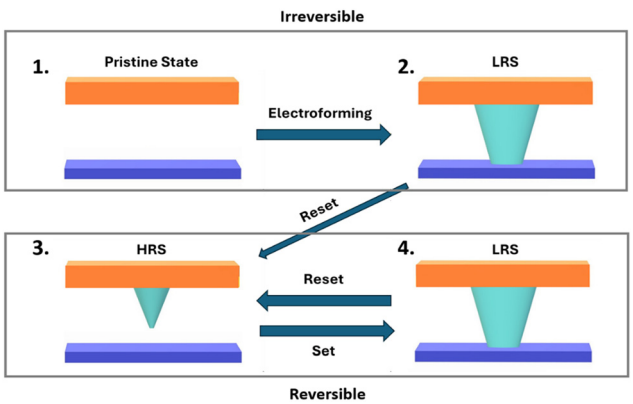

Fig. 1 Schematic illustration of the resistive switching effect.

The main advantages of RRAM over conventional memory devices are its low power consumption, higher memory density and higher operating frequencies.[5] It can also provide a solution to the memory-wall bottleneck inherent to the

[a] University of Tartu, Institute of Physics, W. Ostwaldi 1, 50411 Tartu, Estonia. E-mail: toomas.daniel.viskus@ut.ee
[b] Departamento de Electricidad y Electrónica, E.T.S.I. Telecomunicación, Universidad de Valladolid, Campus 'Miguel Delibes', 47011 Valladolid, Spain

currently used Von Neumann architecture because of the time required to transfer information between memory and processor. In the case of RRAM devices, a single cell can act as both memory storage and a logical switch, thereby removing the signal delay. Additionally, RRAM devices are compatible with complementary metal oxide semiconductor (CMOS) technology due to their simple metal–insulator–metal (MIM) structure. Because of these features, RRAM devices have garnered attention in the quickly advancing fields of neural networks and artificial intelligence.[6–15] To thoroughly evaluate the switching mechanism and the potential of these devices for the aforementioned neuromorphic applications, conductance (G) is universally used as the primary metric to represent synaptic weights when assessing the neuromorphic properties of memristive devices.[16] Therefore, in addition to current–voltage (I–V) characteristics, conductance–voltage (G–V) characteristics are often analyzed, as they directly reflect the insulating properties of the dielectric and the nature of the conductive filament.[17]

There are many types of materials that demonstrate RS properties. Resistive switching has been observed in biological materials,[18,19] polymers[20] and metal oxides such as HfO_2[6,9–11,14,21–31] and TiO_2.[32–35] Regarding RS characteristics of devices utilizing only HfO_2 as a switching layer, Lie *et al.*[36] have shown that depending on the electrodes used in the RS device, the switching could be either bipolar or unipolar. Different combinations of bottom electrode (BE) and top electrode (TE) have been used in bipolar RS devices based on HfO_2.[9,14,26,27,29] These studies have demonstrated that well-controlled interfaces between the RS layer and electrodes play an important role in determining the characteristics of RS devices. For instance, applying a RuO_2 layer as bottom electrode has led to considerable improvements of HfO_2-based RS devices compared to the devices with more common TiN bottom electrodes.[9]

In several studies, TiO_2 and HfO_2 thin films have been combined to improve performance of RRAM devices.[8,23,26,37–39] A TiO_2 layer has been formed between the bottom electrode and HfO_2 by deposition[40] or ozone treatment of TiN bottom electrode.[29] TiO_2 has also been added between two HfO_2 layers[23,39] or between the HfO_2 layer and top electrode.[8,37,38]

While a number of studies utilizing both HfO_2 and TiO_2 in a bi- and tri-layer oxide structures have been published, only few studies have focused on resistive switching in samples with mixed or ternary $Hf_xTi_{1-x}O_y$ films, where $0 \leq x \leq 1$ is the Hf/(Hf + Ti) atomic ratio and $y \approx 2$, as resistive-switching layer.[41–43] For instance, Chakrabarti and Vogel[42] studied TiN/$Hf_xTi_{1-x}O_y$/TiN structures with Hf : Ti ratios of 3 : 1 (x = 0.75) and 1 : 1 (x = 0.5) in the switching layer. They obtained forming-free multilevel RS in the devices with a Hf : Ti ratio of 3 : 1 while the devices remained conducting and, therefore, no RS was observed when the Hf : Ti ratio was 1 : 1.[42] Athena *et al.*[41] investigated RS performance of amorphous $Hf_xTi_yO_z$ thin films with Hf : Ti ratios of 3.14 : 1 (x = 0.76), 2.3 : 1 (x = 0.70), and 1.14 : 1 (x = 0.53) in the Au/Ti/$Hf_xTi_yO_z$/Au structures. It was shown that an increase in the Ti content caused a decrease in forming and switching voltages, increase in the high-resistive state (HRS) current, and a shrinking of the RS memory window. The result indicating that increasing Ti content has a strong negative effect on the RS properties is somewhat surprising because devices with TiO_2 RS layers have demonstrated promising performance in previous studies.[32,34,35] Therefore, we started a research to characterize the properties of $Hf_xTi_{1-x}O_y$ RS layers with $x \leq 0.64$. Significant attention was paid to the effect of the switching-layer phase composition on RS, a topic that has earlier been of significant interest only in a limited number of papers.[21,32–35]

In this work, we investigated devices where the $Hf_xTi_{1-x}O_y$ films were deposited by atomic layer deposition (ALD) onto 5 nm thick RuO_2 bottom electrodes. RuO_2 is a material with relatively high work function forming barriers with sufficiently high conduction band offsets with both HfO_2 and TiO_2.[44,45] The same applies to Pt that was the top electrode material of RS devices studied in this work. Furthermore, based on the results of a previous work,[46] it was expected that quasi-epitaxial growth of $Hf_xTi_{1-x}O_y$ at certain x values might improve the RS performance because of enhanced quality of the interface between the dielectric and bottom electrode. Therefore, in addition to the effect of elemental composition, the influence of switching-layer phase composition on the RS performance was one of the main objectives of this work.

2. Experimental

2.1. Sample preparation

The RS Pt/$Hf_xTi_{1-x}O_y$/RuO_2 structures were deposited onto Si(100) substrates with RuO_2/TiN bottom electrodes (Fig. 2). The RuO_2 and TiN thicknesses were 5 and 10 nm, respectively. Using electron beam evaporation (EBE) and a shadow mask, a 1–2 mm wide and ~50 nm-thick Pt-stripe was deposited onto each sample fabricated for electrical measurements (step 1 in Fig. 2) to ensure reliable electrical contact with the bottom electrode.

After that a $Hf_xTi_{1-x}O_y$ film was synthesized from $TiCl_4$, $HfCl_4$, and H_2O in a low-pressure flow-type ALD reactor described elsewhere.[47] In these experiments (step 2 in Fig. 2), N_2 (99.999%, AS Linde Gas) served as a carrier and purging gas. The $HfCl_4$ source temperature was set at 160 °C to achieve sufficient vapor pressure, while the $TiCl_4$ and H_2O sources were kept at room temperature during the deposition process. The $Hf_xTi_{1-x}O_y$ layers with different elemental compositions were deposited by repeating supercycles that included 1–30 cycles for the synthesis of TiO_2 followed by 1 cycle for the synthesis of HfO_2.

ALD cycle time parameters chosen for the deposition of HfO_2 were 5 s for the $HfCl_4$ pulse, 2 s for the first N_2 purge, 2 s for the H_2O pulse, and 5 s for the second N_2 purge while those applied for the deposition of TiO_2 were 2 s for the $TiCl_4$ pulse, 2 s for the N_2 purge, 2 s for the H_2O pulse, and 5 s for the N_2 purge. All films were grown at a substrate temperature of 350 °C. In more detail, the HfO_2 : TiO_2 cycle ratios and the numbers of supercycles used to deposit films with different compositions are specified in Table 1.

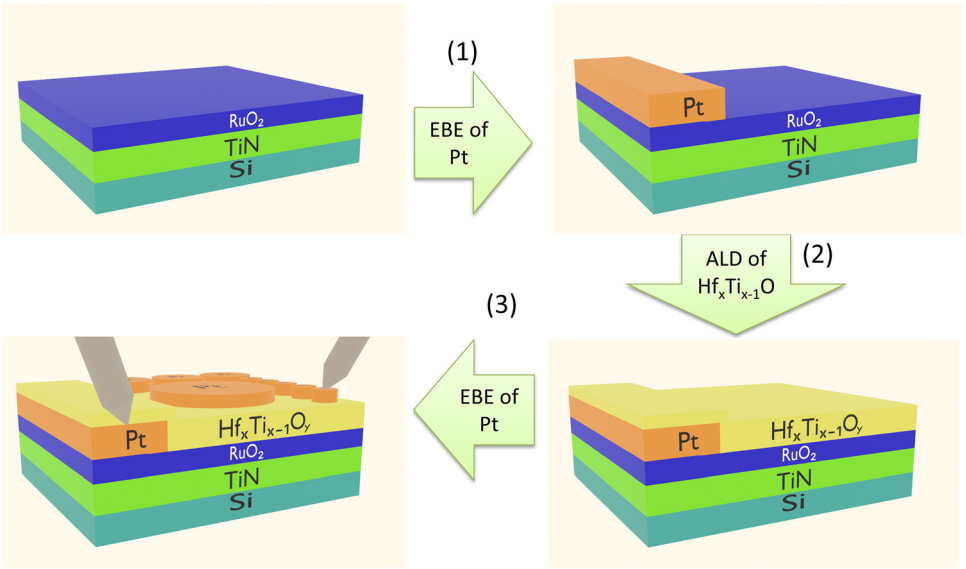

Fig. 2 Main stages of resistive switching sample fabrication.

Table 1 ALD process parameters, Hf/(Hf + Ti) atomic ratios, thicknesses, and growth per cycle values of $Hf_xTi_{1-x}O_y$ films

HfO_2 : TiO_2 cycle ratio	ALD process formula	Hf/(Hf + Ti) atomic ratio	Thickness (nm)	Growth per cycle (pm)
1 : 30	16 (30($TiCl_4$ + H_2O) + ($HfCl_4$ + H_2O))	0.07 ± 0.01	28 ± 3	56 ± 6
1 : 20	24 (20($TiCl_4$ + H_2O) + ($HfCl_4$ + H_2O))	0.11 ± 0.01	29 ± 3	58 ± 6
1 : 10	25 (10($TiCl_4$ + H_2O) + ($HfCl_4$ + H_2O))	0.19 ± 0.02	19 ± 2	69 ± 7
1 : 5	57 (5($TiCl_4$ + H_2O) + ($HfCl_4$ + H_2O))	0.30 ± 0.03	24 ± 3	70 ± 9
1 : 3	80 (3($TiCl_4$ + H_2O) + ($HfCl_4$ + H_2O))	0.36 ± 0.03	22 ± 2	69 ± 7
1 : 2	100 (2($TiCl_4$ + H_2O) + ($HfCl_4$ + H_2O))	0.45 ± 0.04	21 ± 2	70 ± 7
1 : 1	143 (($TiCl_4$ + H_2O) + ($HfCl_4$ + H_2O))	0.64 ± 0.05	19 ± 2	66 ± 7

For electrical measurements, a matrix of 40–60 nm thick Pt top electrodes with circular shapes and areas of 0.20, 0.049, and 0.002 mm^2 were deposited through a shadow mask by EBE (step 3 in Fig. 2). For the characterization of RS properties, the top electrodes with the area of 0.002 mm^2 were used. After the deposition of the top electrodes, the samples studied in this work were annealed at 300 °C for 30 minutes in an O_2 environment. As demonstrated in previous studies, this kind of treatment is necessary to reduce leakage currents, especially for the samples with high TiO_2 concentrations.[45]

2.2. Characterization

For elemental analysis, X-ray fluorescence measurements were carried out with a ZSX-400 (Rigaku) spectrometer. The phase composition of the samples was characterized with a materials research X-ray diffractometer SmartLab™ (Rigaku). Cu K_α radiation (with the wavelength of 0.154178 nm) emitted by a rotating anode, working at 8.1 kW (45 kV, 180 mA), and the grazing incidence X-ray diffraction (GIXRD) mode (angle of incidence $\omega = 0.35°$) were applied for this purpose. The crystalline phases were identified using the X-ray diffraction database PDF-2 (version 2023) of the International Centre of Diffraction Data. The $Hf_xTi_{1-x}O_y$ thicknesses (d) were determined using both the XRF data and X-ray reflection curves measured with the SmartLab™ diffractometer.

Transmission electron microscopy (TEM) studies were performed with a Titan Themis 200 microscope (FEI). The microscope was equipped with a FEI/Bruker energy-dispersive X-ray spectrometer allowing elemental mapping. A lamella for TEM and scanning TEM (STEM) measurements was prepared using a Helios Nanolab 600 SEM-FIB microscope. For protecting the RS device structure, an additional layer of Pt was deposited in the SEM-FIB on the top of the sample before starting the lamella preparation process. After that a lamella was cut, lifted and placed onto a holder, thinned down to the required thickness, and then polished to obtain high-resolution TEM images of the sample cross-section.

Electrical measurements were conducted with a Keithley 2636A source-meter and Cascade Microtech EPS150TRIAX probe station. The probe station was shielded to mitigate electromagnetic interference. Its base plate (chuck) had a heating capability, enabling measurements at elevated temperatures. For electroforming of the conductive filaments (CF) the voltage (V) applied to a device was swept with 0.05 V steps in the positive or negative direction until a breakdown was observed. The breakdown current was controlled by setting the compliance current (I_{cc}) of the source-meter at 0.5–15 mA.

Voltage sweeping with a step of 0.05 V was also used for recording current–voltage (I–V) curves characterizing the RS performance of devices. The I_{cc} levels limiting the current

during the switching of a device from the HRS to the low-resistive state (LRS) ranged from 0.5 to 3 mA. From the *I–V* curves, conductance (*G*) *versus* voltage (*G–V*) curves were derived to illustrate the ohmic (*G* is independent of voltage) or non-ohmic (*G* depends on voltage) character of conductance in CF. Endurance characteristics were studied using 20 ms switching and read pulses. Retention of the LRS and the HRS was studied at temperatures up to 110 °C measuring the current of each state at 0.2 V with intervals of 60 s during 6 hours. In addition, *I–V* characteristics of some devices were measured with a Keithley 4225 pulse measurement unit at pulse durations ranging from 100 ns to 1 ms.

3. Results and discussion

3.1. Elemental and phase composition of $Hf_xTi_{1-x}O_y$

The data presented in Table 1 demonstrate that *x* monotonically increased with the $HfO_2/(HfO_2 + TiO_2)$ ALD-cycle ratio. The dependence was not linear (Fig. S1) because in this *x* range, the atomic growth per cycle of Hf was higher and depended on *x* in a different way compared to that of Ti.[46]

X-ray diffractograms of samples with $Hf_xTi_{1-x}O_y$ films but without top electrodes are depicted in Fig. 3. In the diffractograms of samples with $x < 0.19$ in the $Hf_xTi_{1-x}O_y$ layer, the most intense reflections can be attributed to the rutile phase. These reflections are markedly stronger than those in the diffractogram of a RuO_2/TiN/Si stack with a 15 nm-thick RuO_2 layer, presented as a reference in Fig. 3. Considering that the RuO_2 layer was even thinner (5 nm) in the samples with the $Hf_xTi_{1-x}O_y$ layers, the possible contribution of the rutile-type RuO_2 to the diffractograms of these samples could not be significant. Consequently, the rutile phase was also formed in the $Hf_xTi_{1-x}O_y$ films. With increasing *x*, the rutile reflections shifted to lower 2θ values. The shift was clearly due to formation of a rutile-phase $Hf_xTi_{1-x}O_y$ solid solution where the higher ionic radius (*r*) of Hf^{4+} (r = 86 pm) compared to that of Ti^{4+} (r = 64 pm), caused an increase in bond lengths with increasing *x*.

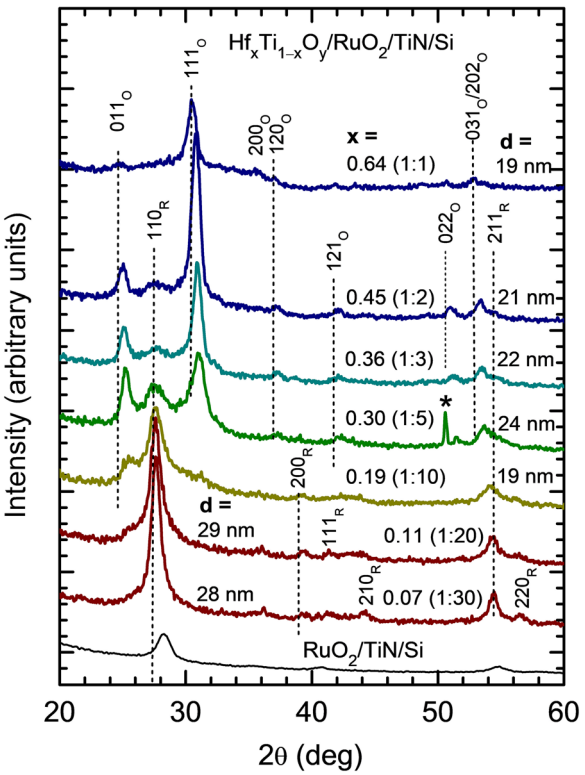

Fig. 3 GIXRD patterns of $Hf_xTi_{1-x}O_y/RuO_2$/TiN/Si structures and RuO_2/TiN/Si stack with a 15 nm-thick RuO_2 layer. The values of *x*, $HfO_2:TiO_2$ cycle ratios, and $Hf_xTi_{1-x}O_y$ thicknesses are shown at the corresponding diffractograms. Miller indices and reflection positions shown for rutile-phase TiO_2 (R) and orthorhombic $HfTiO_4$ (O) correspond to PDF-2 cards 01-089-4202 and 00-040-0794, respectively. A reflection attributable to a substrate or sample stage of diffractometer is marked with an asterisk.

When *x* exceeded 0.19, additional reflections appeared in the diffractograms (Fig. 3). With increasing *x*, the positions of these reflections shifted similarly to those of the rutile reflections. Analysis of the diffractograms led to the conclusion that a crystalline $Hf_xTi_{1-x}O_y$ phase isomorphous with orthorhombic $HfTiO_4$ was responsible for the additional reflections. Notably, an increase in the average growth per cycle (GPC) was observed with the increase of *x* from 0.11 to 0.19 (Table 1). This change in GPC was in correlation with the appearance of orthorhombic phase. However, the higher GPC of HfO_2 compared to that of TiO_2, observed at low *x* values,[46] could also contribute to the increase in the mean GPC with increasing *x*. As the increase in GPC is comparable to the experimental uncertainty, distinguishing of these two effects is unfortunately impossible.

In the *x* range of 0.19–0.45, reflections of both rutile and orthorhombic phases were observable in corresponding X-ray diffractograms (Fig. 3). However, an increase in *x* led to a marked decrease in the intensities of rutile reflections and steep increase in the intensities of reflections attributable to the orthorhombic phase. Consequently, transition from the growth of rutile-phase $Hf_xTi_{1-x}O_y$ to that of orthorhombic $Hf_xTi_{1-x}O_y$ took place, when *x* increased from 0.19 to 0.45. In the diffractograms of samples where $x = 0.64$, the reflections of orthorhombic phase were weaker compared with those in the diffractograms corresponding to $x = 0.45$ (Fig. 3). This result together with an increased background intensity in a 2θ range of 23°–38° indicates that $Hf_xTi_{1-x}O_y$ with relatively poor crystallinity was formed at $x = 0.64$. Transition to the monoclinic crystalline phase isomorphous with monoclinic HfO_2, earlier observed in an *x* range of 0.65–0.75,[46] was a probable reason for this result.

In order to reveal the significance of the bottom electrode in the growth of crystalline phases of $Hf_xTi_{1-x}O_y$, a cross-section of a sample containing a $Hf_xTi_{1-x}O_y$ layer, where $x = 0.36$, was studied by TEM. The results demonstrated that the ALD process caused no noticeable damage to the relatively thin (5 nm) RuO_2 layer (Fig. 4(a)). However, the STEM images (Fig. 4(a)) and line scan data (Fig. 4(b)) indicate that a TiO_xN_y interface layer was formed between the TiN and RuO_2 layers.

High-resolution TEM studies revealed growth of crystalline $Hf_xTi_{1-x}O_y$ starting from the interface between crystalline RuO_2

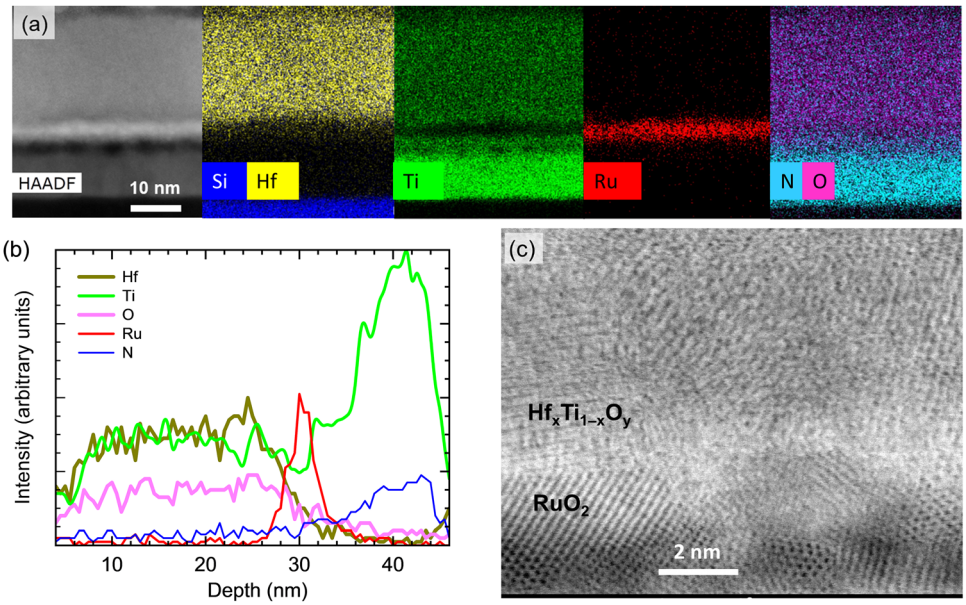

Fig. 4 (a) Transmission electron microscopy image and STEM elemental composition maps, (b) elemental composition profiles, and (c) high-resolution TEM image of a Pt/$Hf_xTi_{1-x}O_y$/RuO_2/TiN/Si structure with x = 0.36 in the $Hf_xTi_{1-x}O_y$ layer.

and $Hf_xTi_{1-x}O_y$ (Fig. 4(c)). This result is in line with the data of recent studies, showing that RuO_2 seed layers are able to stimulate growth of rutile and orthorhombic phases of $Hf_xTi_{1-x}O_y$.[46] As discussed in a recent paper,[46] epitaxial growth of rutile and orthorhombic phases of $Hf_xTi_{1-x}O_y$ on rutile-phase RuO_2 is one possible reason for this effect. First, the rutile phase of RuO_2, supporting the growth of rutile-phase TiO_2,[48] can also stimulate the growth of rutile-phase $Hf_xTi_{1-x}O_y$ provided that x is small and the unit cell parameters of $Hf_xTi_{1-x}O_y$ are close to those of RuO_2. Second, the crystal structures of orthorhombic $HfTiO_4$ (PDF card 00-040-0794) and orthorhombic TiO_2-II (PDF-2 card 21-1238) are similar in both space group symmetry and unit cell parameters while TiO_2-II is able to form lattice-matched structures with the rutile phase of TiO_2.[49] Hence, orthorhombic $Hf_xTi_{1-x}O_y$ and rutile-phase $Hf_xTi_{1-x}O_y$ or orthorhombic $Hf_xTi_{1-x}O_y$ and rutile-phase RuO_2 could also form lattice-matched structures making possible the epitaxial growth of orthorhombic $Hf_xTi_{1-x}O_y$ directly on RuO_2 or on rutile-phase $Hf_xTi_{1-x}O_y$ formed on RuO_2. However, the TEM image depicted in Fig. 4(c) indicates that epitaxial growth is not the predominant mechanism leading to the growth of crystalline phases in $Hf_xTi_{1-x}O_y$ films studied in this work. A similar substrate-stimulated growth of non-epitaxial crystalline phases has earlier been observed during deposition of Ga_2O_3 on Ru seed layers.[50,51] In these reports, impact of surface morphology on nucleation has been suggested to be the main reason for the preferential crystallization of Ga_2O_3 on Ru seed layers. Thus, the same effect could also be responsible for the growth of crystalline $Hf_xTi_{1-x}O_y$ on RuO_2.

3.2. Influence of $Hf_xTi_{1-x}O_y$ composition on forming characteristics

In the whole composition range of $Hf_xTi_{1-x}O_y$, studied in this work, bipolar RS was obtained. All RS devices studied switched to the LRS at the negative polarity and to the HRS at positive polarity of the voltage applied to the top electrode. This kind of switching was predominantly observed even if the conductive filament was formed at the positive voltage polarity (Fig. 5(a)). As can be seen by comparing the I–V curves recorded during the CF electroforming (Fig. 5(a and b)), at similar absolute values of voltages applied to the top electrode, the current values were much higher, when a positive voltage was applied to the top electrode (Fig. 5(a)). In the latter case, electrons were injected into the $Hf_xTi_{1-x}O_y$ layer from the RuO_2 bottom electrode. In the opposite case, when the negative polarity of voltage was applied to the top electrode, the electrons were injected to $Hf_xTi_{1-x}O_y$ from the Pt top electrode. Thus, as suggested in an earlier publication where electrical characteristics of RuO_2/TiO_2/RuO_2 and Pt/TiO_2/RuO_2 structures were studied,[45] this kind of difference in leakage currents was evidently caused by the lower work function of RuO_2 compared with that of Pt. As a result, relatively high I_{cc} levels were needed to see dielectric breakdown at the positive top electrode voltage polarity (Fig. 5(a)).

For example, no evidence of breakdown was observed when I_{cc} was set at 10 mA, and the voltage was swept from 0 to 11.2 V (curve 1 in Fig. 5(a)). Nevertheless, when I_{cc} was increased to 15 mA and the voltage was swept from 0 to 11.7 V (curve 1′ in Fig. 5(a)), the breakdown was clearly observable at 10.7 V, that is, at a voltage that was lower than the stop value of the first sweep. In addition, markedly higher current values were recorded during the second sweep (curve 1′) than during the first one (curve 1). Therefore, the formation of a conductive channel through the dielectric was obviously initiated already during the first sweep. When the voltage was swept from 11.7 V to −2 V (curves 2 and 3 in Fig. 5(a)), additional switching to an even lower resistance level occurred at −1.4 V. After that RS

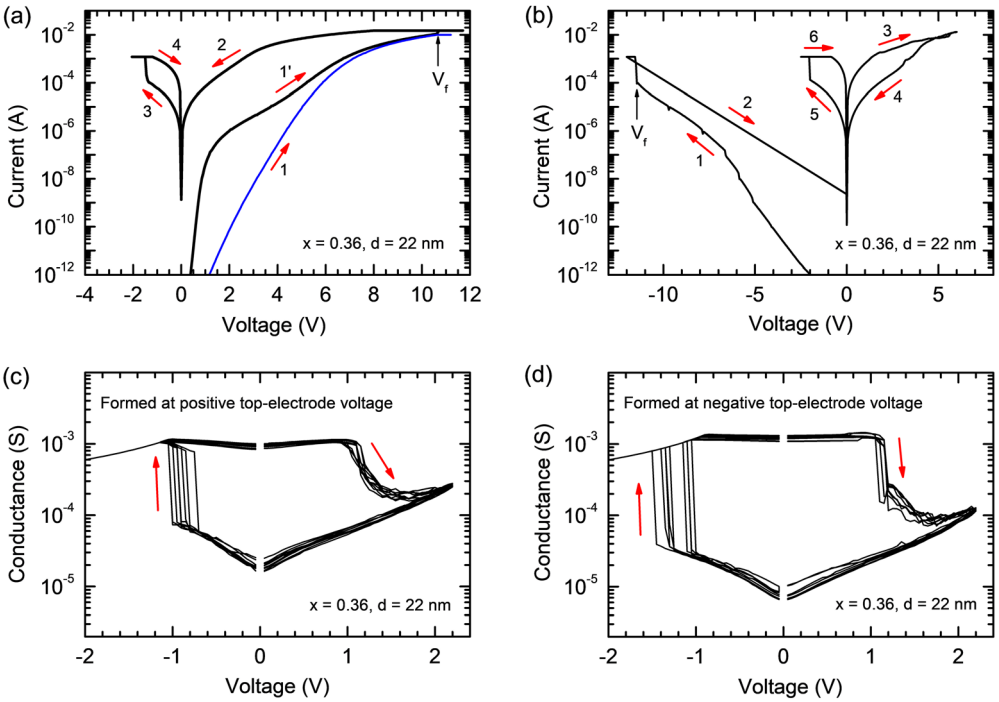

Fig. 5 (a) and (b) Current–voltage characteristics recorded during the electroforming of conductive filaments by applying (a) positive and (b) negative voltage to the top electrode. (c) and (d) Conductance-voltage curves of RS devices formed at (c) positive and (d) negative top-electrode voltages.

with reset (switching to the HRS) at positive voltages and set (switching to the LRS) at negative top electrode voltages was established as demonstrated by the conductance *versus* voltage (G–V) characteristics presented in Fig. 5(c).

Electroforming was obtained at markedly lower pre-breakdown currents, when voltage with negative polarity was applied to the top electrode (curve 1 in Fig. 5(b)). After switching the voltage to 0 (line 2 in Fig. 5(b)) and sweeping to 6 V, gradual switching to the HRS was observed (curves 3 and 4 in Fig. 5(b). During the next voltage sweep to the negative direction (curve 5 in Fig. 5(b)), the sample switched to the LRS at −1 V. After a few following cycles, the RS described in Fig. 5(d) was stabilized.

Owing to the lower pre-breakdown current values, it was possible to use lower values and wider range of I_{cc} during the CF forming at negative top electrode voltage polarity (Fig. 5(a and b)). Considering that wider range of possible I_{cc} levels allowed more flexible control of CF formation, negative forming polarity was used for all RS structures characterized in this work (Fig. 5(b) and 6(a, b)) while forming at positive top electrode voltages was studied only in the case of a few structures (Fig. 5(a) and 6(b)). As the forming voltage (V_f) depended on the RS layer thickness, the mean electric field $E = V/d$ was used to characterize the influence of the $Hf_xTi_{1-x}O_y$ composition on the CF formation (Fig. 6(a and b)). The data presented in Fig. 6 show a steep increase of the breakdown electric field strength (E_B) from 2.1–3.1 MV cm^{-1} to 4.7 MV cm^{-1} with the x increase from 0.11 to 0.19. In the same composition range, the content of rutile phase decreased and the orthorhombic phase of $Hf_xTi_{1-x}O_y$ appeared in the films

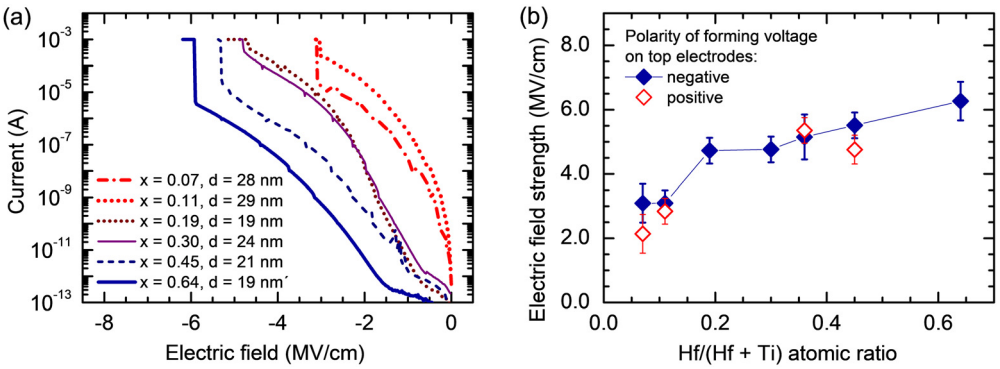

Fig. 6 (a) Current as a function of electric field of samples with different compositions of $Hf_xTi_{1-x}O_y$ layers and (b) influence of Hf/(Hf + Ti) atomic ratio on the electric field strength, needed for CF forming in $Hf_xTi_{1-x}O_y$.

(Fig. 3). In contrast, significantly slower increase (from 4.7 to 6.3 MV cm^{-1}) in E_B was observed with a further increase of x from 0.19 to 0.64. Studies of $Hf_xTi_{1-x}O_y$ layers with x values of 0.07, 0.11, 0.36, and 0.45 revealed that at these compositions, the voltage polarity had no significant effect on the mean E_B values (Fig. 6(b)). Comparing the data presented in Fig. 6(b) with the breakdown voltages reported for 5 nm-thick amorphous $Hf_xTi_{1-x}O_y$ films,[41] one can see that at similar compositions, E_B values of the films containing the orthorhombic phase are considerably (by a factor of 1.3–1.4) higher than those of the amorphous films.

3.3. Resistive switching at room temperature

I–V-Characteristics of RS devices (Fig. 7(a and b) and Fig. S2, S3(a)) most significantly depended on the $Hf_xTi_{1-x}O_y$ composition in the x range of 0.19–0.30. Both set and, particularly, reset transitions that were gradual at x ranging from 0.07 to 0.19 became steeper when x increased to 0.30 (Fig. 7(b)). Consequently, a strict and lower I_{cc} was sometimes imposed for the samples with $x \geq 0.30$ (Fig. S3(a and b)) to prevent the irreversible breakdown of the oxide layer during the abrupt set transitions, whereas samples with lower x required higher I_{cc} to exhibit a more stable memory window (Fig. S4(a and b)). No significant changes in the shapes of the *I–V* curves were observed with the increase of x from 0.30 to 0.64, although $I_{LRS}/I_{HRS} = G_{LRS}/G_{HRS}$, where I_{LRS} and I_{HRS} are the current, and G_{LRS} and G_{HRS} are the conductance values in the LRS and HRS, respectively, increased with x in this composition range as well (Fig. 7(b–d)).

Another effect, observed in the x range of 0.07–0.19, was a considerable dependence of G_{LRS} on voltage in the voltage range where no switching processes occurred (Fig. 7(c)). By contrast, at $x \geq 0.30$, this type of dependence was weak or negligible (Fig. 5(c, d), 7(c) and Fig. S3(b)), indicating formation of CF with nearly ohmic conductance in $Hf_xTi_{1-x}O_y$ layers with compositions enabling growth of orthorhombic phase (Fig. 3). Fig. 8(a) confirms that the behavior in the LRS state was ohmic for the values of x ranging from 0.30 to 0.64. In the voltage range shown in Fig. 8(a), the standard deviations of linear fittings were 0.48%, 0.23%, and 0.011% for the samples with x of 0.30, 0,36 and 0.64, respectively.

Stronger dependence of G_{LRS} on voltage, typical for films with $x \leq 0.19$ (Fig. 7(c)), was probably related to lower concentration of oxygen vacancies in CF formed in the rutile phase that was the predominant one in $Hf_xTi_{1-x}O_y$ with $x \leq 0.19$ (Fig. 3). Higher stability of rutile compared to that of the orthorhombic phase could be a reason for this effect. It should also be noted, that G_{LRS}, determined at voltages ranging from −0.5 to 0.5 V, markedly increased with the x increase from 0.19 to 0.30 (Fig. 7(c)). This result supported the conclusion that CF with high concentrations of oxygen vacancies were more easily obtained in orthorhombic $Hf_xTi_{1-x}O_y$ than in rutile-phase $Hf_xTi_{1-x}O_y$.

The increase in G_{LRS} is obviously beneficial for obtaining higher G_{LRS}/G_{HRS}. However, the increase in G_{LRS} with increasing x was obsered only at $x \leq 0.36$ (Fig. 7(c)). At $x \geq 0.36$, the increase in G_{LRS}/G_{HRS} was mainly due to the corresponding decrease in G_{HRS} (Fig. 7(c)) that was in line with the increase in

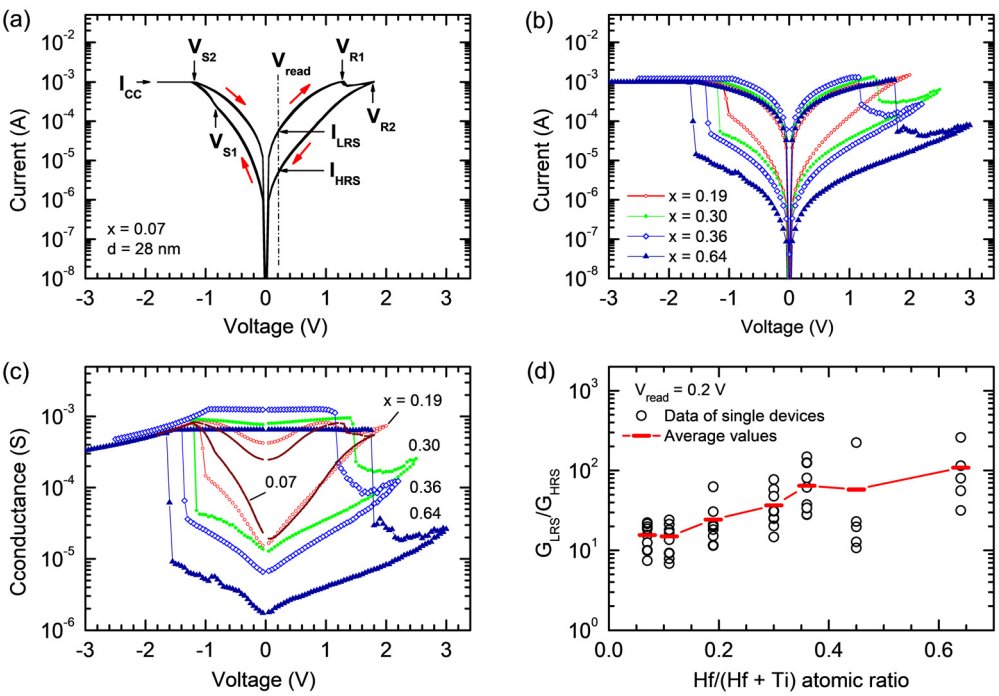

Fig. 7 Resistive switching characteristics of $Hf_xTi_{1-x}O_y$ layers with different compositions. (a) Current–voltage characteristics of a layer with x of 0.07 (b) representative current–voltage characteristics of films where $0.19 \leq x \leq 0.64$, (c) representative conductance-voltage characteristics of films where $0.07 \leq x \leq 0.64$, and (d) G_{LRS}/G_{HRS} determined at V_{read} = 0.2 V as a function of Hf/(Hf + Ti) atomic ratio.

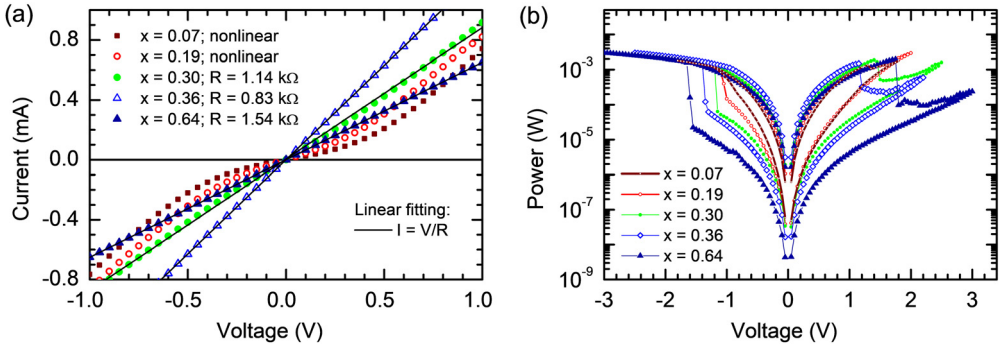

Fig. 8 (a) LRS current–voltage curves of RS structures with different $Hf_xTi_{1-x}O_y$ compositions and linear fitting the curves of samples with x of 0.30, 0.36 and 0.64 at voltages ranging from −1 to 1 V. (b) Power–voltage characteristics of RS structure with different $Hf_xTi_{1-x}O_y$ compositions.

the bandgap energy of $Hf_xTi_{1-x}O_y$ and energy barrier height at the interface between bottom electrode and $Hf_xTi_{1-x}O_y$ with increasing x.[52] A similar influence of composition on G_{HRS} and RS memory window has been observed in an x range of 0.53–1 by Athena *et al.*[41] At the same time, the average values of memory windows obtained in our experiments for samples with x ranging from 0.30 to 0.64 (Fig. 7(d)) noticeably exceeded those earlier reported for $Hf_xTi_{1-x}O_y$ RS layers with x = 0.53 and x = 0.70.[41] One possible reason for this difference is the dissimilar phase compositions of RS layers. Unlike our work, amorphous $Hf_xTi_{1-x}O_y$ films were studied in the earlier one.[41] Additionally, electrodes with high work functions contributed to relatively high G_{LRS}/G_{HRS} ratios observed in our experiments.

To further evaluate the efficiency of the RS devices, the power consumption ($P = I{\cdot}V$) was calculated from the current–voltage characteristics. Fig. 8(b) displays the representative power–voltage (P–V) curves showing that in LRS, the maximum power consumption was similar for all configurations and was in the order of milliwatts. In contrast, the power consumption in HRS decreased by more than an order of magnitude when x increased from 0.07 to 0.64. The increase in x also caused a marked reduction in the power required for transitions from HRS to LRS (Fig. 8(b)).

The RS parameters V_{S1}, V_{S2}, V_{R1}, and V_{R2} (Fig. 7(a)), corresponding to the voltages, at which the set (V_{S1} and V_{S2}) and reset (V_{R1} and V_{R2}) started (V_{S1} and V_{R1}) and were completed (V_{S2} and V_{R2}), can be found in Table 2. The average values depicted in Table 2 were determined from I–V characteristics recorded at I_{cc} ranging from 0.8 to 1.2 mA as at these I_{cc} values, reliable RS was obtained in all $Hf_xTi_{1-x}O_y$ layers. I–V Curves recorded at similar I_{cc} range were used for this purpose because the switching voltages significantly depended on I_{cc} (Fig. S4(a–d)). For example, the increase of I_{cc} from 1 to 3 mA caused an increase in V_{R1} by a factor of 1.2, approximately. By contrast, the same increase in I_{cc} had a markedly weaker effect on the I_{LRS}/I_{HRS} ratio (Fig. S4).

The lowest absolute values of switching voltages were measured for $Hf_xTi_{1-x}O_y$ layers with x ranging from 0.07 to 0.36 (Table 2). In this range, the variations in switching voltages, related to the increase in x, did not exceed the experimental uncertainty. A significant increase in switching voltage amplitudes was observed with the increase of x to 0.64. This kind of increase in switching voltage amplitudes is in a good agreement with that observed in the same composition range by Athena *et al.*[41] It is also worth noting that switching voltages, determined for $Hf_xTi_{1-x}O_y$ RS layers with x of 0.07–0.19, were similar to those determined for RS devices with RuO_2 and Pt electrodes and TiO_2–$Ti_xAl_{1-x}O_y$ RS layers where the Al/(Al + Ti) atomic ratios ranged from 0.026 to 0.13.[53]

The results of endurance tests are displayed in Fig. 9(a–d). In all cases, the endurance measurements were stopped when a significant decrease in the I_{LRS}/I_{HRS} ratio was observed. Therefore, different ranges of RS cycles are shown for different $Hf_xTi_{1-x}O_y$ compositions in Fig. 9(a–c). A general trend that can be seen in Fig. 9 is a marked improvement in endurance characteristics with the increase of x from 0.19 to 0.30. This kind of performance can also be related to the appearance of the orthorhombic phase of $Hf_xTi_{1-x}O_y$ in the RS layers (Fig. 3).

In order to understand possible reasons and mechanisms responsible for the degradation of RS devices (Fig. 9(a–c)), G–V

Table 2 Resistive switching voltages of $Hf_xTi_{1-x}O_y$ films with different Hf/(Hf + Ti) atomic ratios

Hf/(Hf + Ti) atomic ratio	V_{S1} (V)	V_{S2} (V)	V_{R1} (V)	V_{R2} (V)
0.07 ± 0.01	−0.90 ± 0.09	−1.24 ± 0.18	1.18 ± 0.17	1.88 ± 0.21
0.11 ± 0.01	−0.82 ± 0.07	−1.12 ± 0.20	1.09 ± 0.21	1.59 ± 0.18
0.19 ± 0.02	−1.04 ± 0.18	−1.24 ± 0.26	1.04 ± 0.11	1.97 ± 0.14
0.30 ± 0.03	−0.95 ± 0.18	−1.31 ± 0.17	1.27 ± 0.18	2.27 ± 0.09
0.36 ± 0.03	−0.99 ± 0.16	−1.27 ± 0.14	1.15 ± 0.11	2.03 ± 0.12
0.45 ± 0.04	−1.17 ± 0.07	−1.52 ± 0.19	1.58 ± 0.31	1.95 ± 0.10
0.64 ± 0.05	−1.50 ± 0.09	−1.72 ± 0.07	1.68 ± 0.17	2.91 ± 0.09

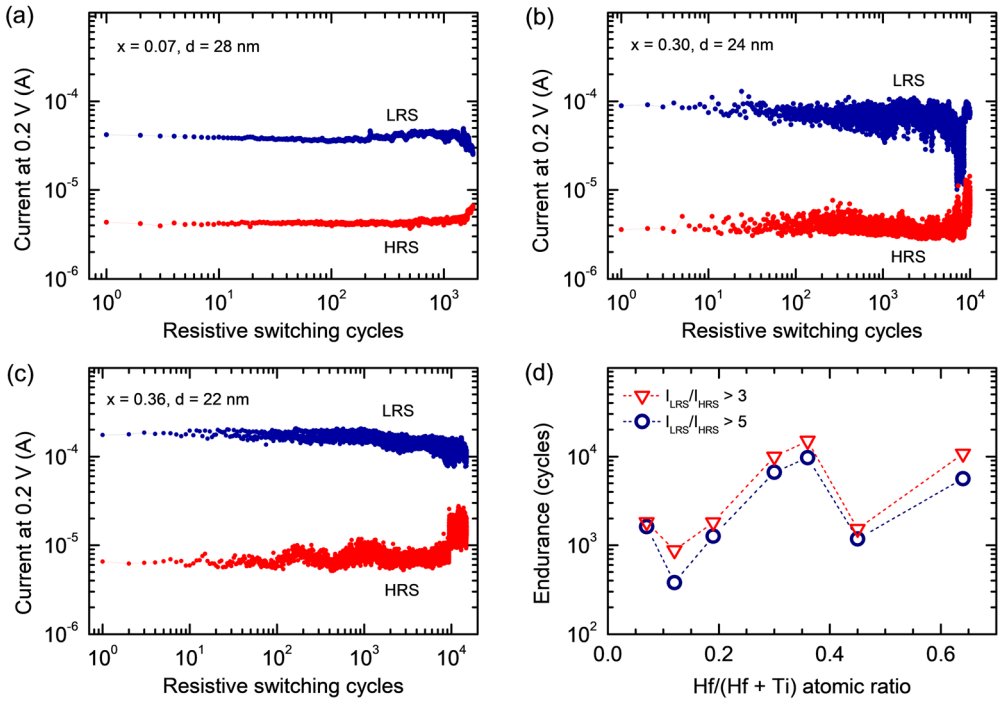

Fig. 9 (a)–(c) Endurance characteristics of RS devices with Hf/(Hf + Ti) atomic ratios of (a) 0.07, (b) 0.30, and (c) 0.36 in $Hf_xTi_{1-x}O_y$, and (d) endurance as a function of Hf/(Hf + Ti) atomic ratio in $Hf_xTi_{1-x}O_y$.

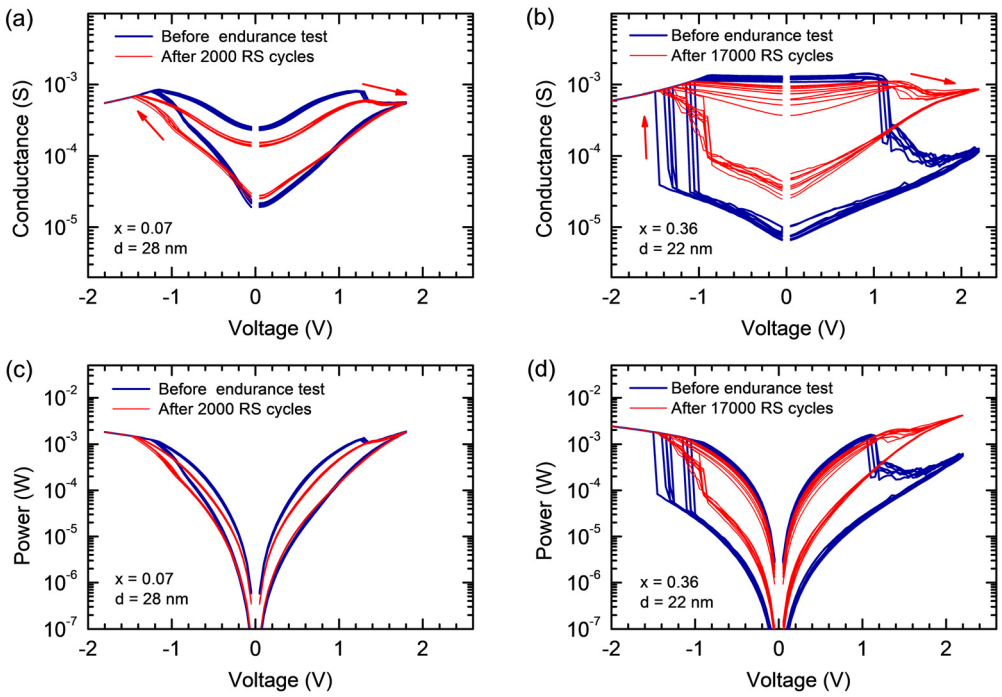

Fig. 10 (a) and (b) Conductance–voltage and (c) and (d) power–voltage characteristics determined before and after endurance tests for devices containing RS $Hf_xTi_{1-x}O_y$ layers with x of (a) and (c) 0.07 and (b) and (d) 0.36.

characteristics (Fig. 10(a, b) and Fig. S5(a, b)) were recorded before the endurance tests and after significant shrinking of memory window. Comparison of G–V curves indicated that the set and reset start voltages (V_{S1} and V_{R1}, respectively) did not change significantly during the endurance tests. In contrast, the set and, particularly, the reset processes became more gradual. The latter effect led to a shrinking of memory window with increasing number of RS cycles in the case of all samples

described in Fig. 10 and Fig. S5. An interesting result is that a decrease in the CF conductivity in LRS seems to be a reason for degradation of samples with low x values (Fig. 10(a)) while an increase in the CF conductivity in HRS causes the decrease in the I_{LRS}/I_{HRS} ratio of the samples where $x \geq 0.30$ (Fig. 10(b) and Fig. S5(a, b)).

The reduction of CF conductivity in LRS of samples with low x values in $Hf_xTi_{1-x}O_y$ could be explained by the decreasing ability of the bottom electrode to absorb oxygen during the set process or by the increasing strength of oxygen bonding in $Hf_xTi_{1-x}O_y$ with rutile structure. However, both hypotheses require verification in further studies.

Inefficient recovery of the oxygen concentration needed for complete rupture of CF during the reset process, was a possible reason for the more gradual reset and increased HRS conductivity determined for $Hf_xTi_{1-x}O_y$ layers with x of 0.3–0.64 after endurance tests (Fig. 10(b) and Fig. S5(b)). This can be related to gradual removal of oxygen from the vicinity of CF or irreversible oxygen bonding in the bottom electrode serving as an oxygen reservoir in our RS structures. Alternatively, the generation of additional defects in or near the CF region could also cause an increase in leakage current, making it more difficult or even impossible to recover the initial resistance of the device in its HRS.

It is also important to note that the power required to complete the set and/or reset transitions increased due to degradation of RS structures (Fig. 10(c, d) and Fig. S5(c, d). At small x values (x = 0.07) more power was needed for both set and reset processes (Fig. 10(c)) while at x values of 0.30–0.64, only the power required to complete the reset transition increased (Fig. 10(d) and Fig. S5(c,d)).

3.4. Resistive switching and retention at elevated temperatures

Resistive switching characteristics of samples with x of 0.36 in $Hf_xTi_{1-x}O_y$, demonstrating superior performance at room-temperature, were also studied at temperatures up to 140 °C. The I–V characteristics of a device, formed at room temperature, were measured at 25, 50, 80, 100, 120, and 140 °C, and then at 120, 100, 65, and 25 °C. At each temperature 10–20 RS cycles were recorded using a compliance current of 1.2 mA. The results of these studies are summarized in Fig. 11.

I–V Curves recorded at voltages ranging from −2.2 to 2.5 V (Fig. 11(a–c)) demonstrate significant decrease in the I_{LRS}/I_{HRS} ratio with the temperature increase from 25 to 140 °C. In addition, differently from the I–V curves measured at room temperature before heating the sample (Fig. 11(a)), the I–V curves recorded at 140 °C (Fig. 11(b)) did not show abrupt current changes during the set and reset transitions. Comparing the data depicted in Fig. 11(a and c), one can see that the initial shape of I–V curves was only partially recovered when the sample was cooled down to 25 °C. In particular, the measurements at elevated temperatures resulted in more stable RS characteristics but a narrower memory window at 25 °C compared to those determined before the high-temperature measurements (Fig. 11(a and c)). Some changes, caused by the RS cycling at elevated temperatures, for instance, inhibition of the reset transition leading to shrinking of memory window, were very similar to those

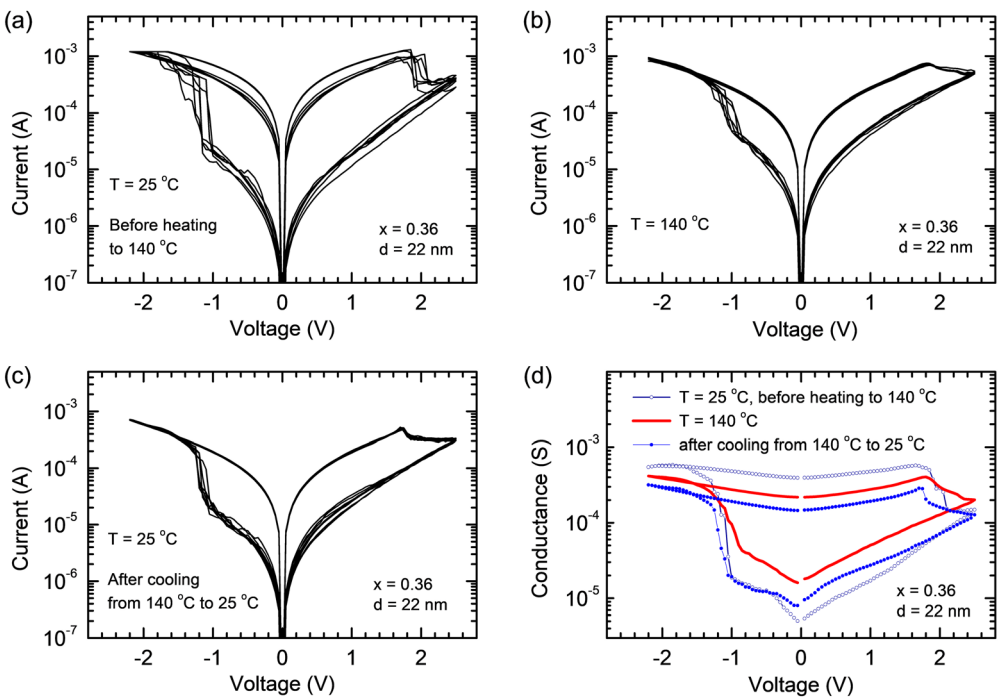

Fig. 11 (a)–(c) I–V Characteristics of a RS structure with x = 0.36 recorded (a) at 25 °C before heating to 140 °C, (b) at 140 °C, and (c) at 25 °C after cooling the sample from 140 to 25 °C, and (d) respective average G–V characteristics.

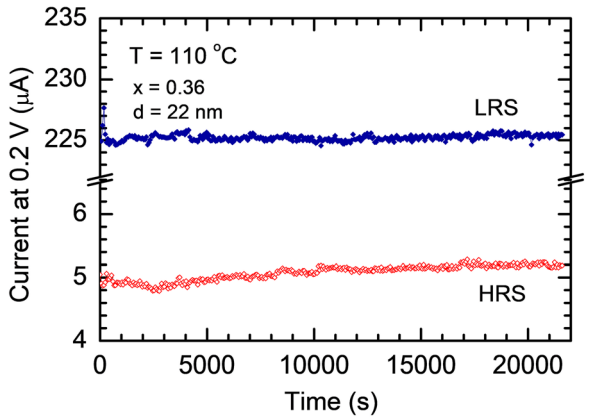

Fig. 12 Retention characteristic measured at 110 °C for a RS structure with x = 0.36.

observed during the endurance tests (Fig. 10(b–d)). Expectedly, these effects appeared much faster during the I–V measurements at elevated temperature than during the endurance tests conducted in the pulse mode at room temperature. Compensation of the memory window shrinking was possible by increasing the reset stop voltage (Fig. S6) as the inhibited reset transition was one of the main reasons for decrease in the I_{LRS}/I_{HRS} (and G_{LRS}/G_{HRS}) ratio (Fig. 11(a–d)). However, increased reset voltages also led to faster degradation of devices.

Another effect influencing the memory window was a considerable decrease in the LRS conductivity during the measurements at elevated temperatures as illustrated by the average G–V characteristics (Fig. 11(d)). This is a notable result because, in all cases shown in Fig. 11, the negative voltage applied was sufficient to completely switch the device into LRS. Therefore, it is possible that the RS cycling at higher temperatures caused formation of more stable oxygen bonds in the CF region, reducing the concentration of oxygen vacancies that can be created during the set process. Alternatively, shrinking the cross section of the CF and/or an increase in the bottom electrode resistance in the vicinity of CF, for example, due to the irreversible oxidation of TiN layer, could also explain the decrease in the LRS conductance.

Retention characteristics measured at 110 °C (Fig. 12) demonstrated marked stability of both HRS and LRS during 6 hours (21 600 s). The most significant changes in I_{LRS} occurred during the first few hundred seconds, when a fluctuation with an amplitude of 2.5 μA was recorded. After that, I_{LRS} remained stable at 225.2 ± 0.8 μA (Fig. 12).

The values of I_{HRS} varied more considerably during the first 10 000 s, when I_{HRS} increased from 4.90 ± 0.10 μA to 5.10 ± 0.05 μA. For comparison, the further increase in I_{HRS} during the next 10 000 s did not exceed 0.1 μA (Fig. 12).

3.5. Resistive switching in pulse mode

The main results of pulse-mode studies of a sample with x = 0.36 in the RS $Hf_xTi_{1-x}O_y$ layer are depicted in Fig. 13 and Fig. S7. As can be seen in Fig. 13(a) and Fig. S7(a–f), RS was obtained at pulse durations down to 100 ns. However, the memory window significantly shrank with decreasing pulse duration, especially at pulse durations <160 ns (Fig. 13(a, d) and Fig. S7(a, b)). Simultaneously, the set and reset transitions

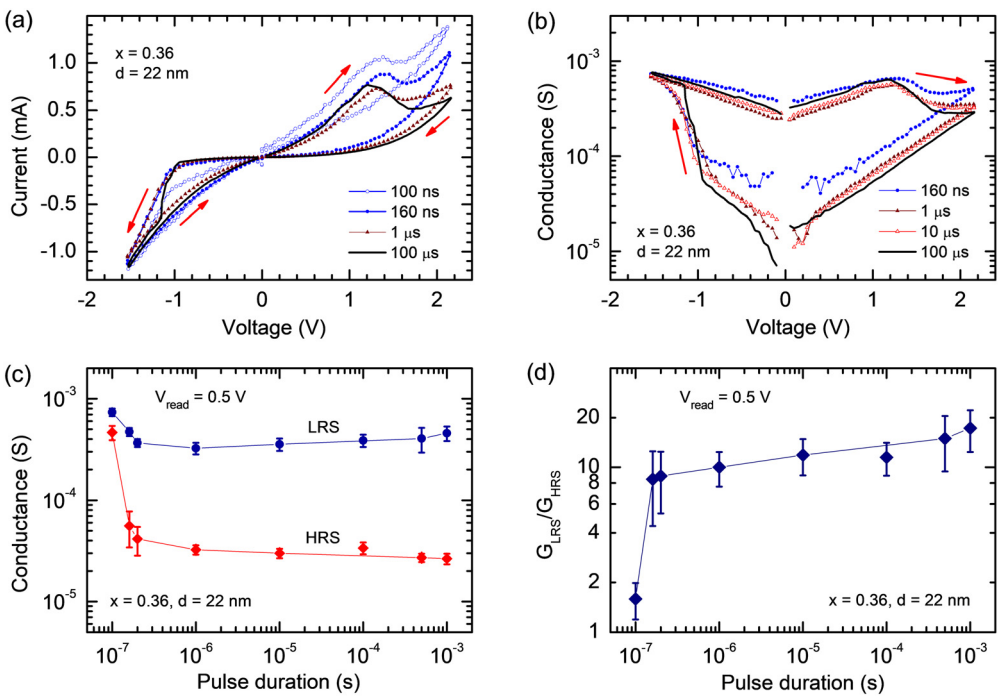

Fig. 13 Influence of pulse duration on average (a) I–V and (b) G–V characteristics, (c) G_{LRS} and G_{HRS}, and (d) G_{LRS}/G_{HRS} of a RS device with x = 0.36 in the RS $Hf_xTi_{1-x}O_y$ layer. (c) and (d) G_{LRS}, G_{HRS}, and G_{LRS}/G_{HRS} were determined at a voltage of 0.5 V.

became more gradual (Fig. 13(a, b) and Fig. S7(a–f)) and G_{HRS} increased with decreasing pulse width (Fig. 13(b and c)).

Notably, instant set transitions that occurred at pulse durations $\geq$100 μs (Fig. S7(e and f)) were not recorded at $\leq$10 μs (Fig. S7(a–d). Thus, several successive pulses were needed for the set transition at the pulse durations $\leq$10 μs. This result indicates that the charge (and energy) supplied by a single pulse was insufficient for recovering CF in the set process.

The reset transition, being gradual in the whole range of pulse durations, also became slower with decreasing pulse duration (Fig. 12(b) and Fig. S7)). As a result, the I_{HRS} and G_{HRS} values obtained at a reset stop voltage fixed at 2.15 V significantly increased with decreasing pulse duration (Fig. 13(a–c)), causing a decrease in the G_{LRS}/G_{HRS} ratio (Fig. 13(d)).

Fig. 13(c) shows that a marked increase in G_{LRS} appeared together with the steep increase in G_{HRS}, when the pulse duration decreased from 200 to 100 ns. This increase in G_{LRS} was probably due to incomplete reset, leaving more oxygen vacancies in CF in its HRS, and respectively, allowing more complete removal of oxygen from CF during the following set process.

Proceeding from this data, one can conclude that reset, rather than set, is the process limiting the minimum pulse widths that can be applied for RS of devices studied in the present work. This conclusion is in line with the results of Pérez *et al.*,[54] who investigated TiN/Al:HfO_2/Ti/TiN RS structures and revealed that much more energy is required to complete the reset process. However, Fig. 13(a, b) and Fig. S7(a–e) show that the voltage amplitude required to complete the set transition also increased when the set pulse durations decreased from 100 μs to 100 ns. Notably, this increase in the set voltage amplitude was well comparable to the corresponding parameter reported by Pérez *et al.* for Al:HfO_2 based RS structures in the same range of pulse durations.[54] Our results also agree with the data of García *et al.*,[55] who demonstrated that, due to the incapability of ions to follow fast changes in the electric field, higher ramp rates of switching voltage require higher voltage amplitudes to complete the set and reset transitions. Therefore, careful tuning of the electrical stimulus is essential for stable operation of this kind of memory devices in the nanosecond range.

4. Conclusion

Atomic layer deposition of hafnium–titanium-oxide with Hf/(Hf + Ti) atomic ratios of x = 0.07–0.64 on RuO_2/TiN bottom electrodes allowed growth of crystalline films predominantly containing rutile phase at $x \leq 0.19$ and orthorhombic phase isomorphous with that of $HfTiO_4$ at $0.30 \leq x \leq 0.64$. Complex studies of Pt/$Hf_xTi_{1-x}O_y$/RuO_2/TiN structures demonstrated that both the elemental and in particular the phase compositions markedly influenced the electrical properties of $Hf_xTi_{1-x}O_y$. The studies revealed that the electric field strength required for the initial formation of the CF increased with x while the most significant increase in breakdown electric field strength was observed in the composition range where the transition from the rutile to orthorhombic phase took place.

Independently of the forming voltage polarity, clockwise bipolar RS was obtained in all structures. However, superior RS characteristics were recorded for structures based on $Hf_xTi_{1-x}O_y$ layers containing the orthorhombic phase. The rutile phase is more stable, so the probability of creating oxygen vacancies is lower in rutile than in the orthorhombic phase, in which conducting filaments may be stronger. The samples with $x \geq 0.36$ in the $Hf_xTi_{1-x}O_y$ layer demonstrated LRS/HRS conductance ratios exceeding 100. Endurance exceeding 10^4 RS cycles was measured for samples with x = 0.36 in $Hf_xTi_{1-x}O_y$. In the case of latter samples, RS with the LRS/HRS conductance ratios exceeding 10 was obtained at temperatures up to 140 °C. Retention measurements conducted at 110 °C for 6 hours showed excellent LRS and HRS stability.

Comparison of *I–V* and *G–V* characteristics, recorded before and after endurance tests, as well as before and after measurements at elevated temperatures, indicated that an increase in the voltage amplitude and power, required to complete the reset process, was the main effect leading to the shrinking of memory window during these experiments. A similar effect, that is, increase in the voltage amplitude required to complete the reset process with decreasing duration of switching pulses, was shown to be a reason limiting the application of the RS structures in high-speed memory devices.

Author contributions

Toomas Daniel Viskus: writing – original draft, writing – review & editing, data curation, investigation, conceptualization; Lauri Aarik: writing – review & editing, investigation, supervision; Tõnis Arroval: writing – review & editing, investigation; Aarne Kasikov: writing – review & editing, investigation; Joonas Merisalu: writing – review & editing, software, supervision; Jekaterina Kozlova: investigation; Markus Otsus: writing – review & editing, investigation; Hugo Mändar: writing – review & editing, investigation; Jaan Aarik: writing – original draft, writing – review & editing, conceptualization; Guillermo Vinuesa: writing – review & editing, investigation; Salvador Dueñas: writing – review & editing, funding acquisition; Helena Castán: writing – review & editing, funding acquisition; Kaupo Kukli: writing – review & editing, project administration, supervision, funding acquisition

Conflicts of interest

There are no conflicts to declare.

Data availability

Data is available upon request from the authors.

Supplementary information (SI) containing Fig. S1–S7 is available. See DOI: https://doi.org/10.1039/d6tc00262e.

Acknowledgements

The authors are thankful to Alma-Asta Kiisler for technical assistance. The work was supported by Estonian Research Council (grant PRG2594) and the Estonian Ministry of Education and Research through the Center of Excellence in Sustainable Green Hydrogen and Energy Technologies (grant TK210U5), and partially developed under Grant PID2022-139586NB-C43 funded by MCIN/AEI/10.13039/501100011033 and by ''ERDF A way of making Europe''.

References

1 W. Banerjee, A. Kashir and S. Kamba, Hafnium Oxide (HfO_2) – A Multifunctional Oxide: A Review on the Prospect and Challenges of Hafnium Oxide in Resistive Switching and Ferroelectric Memories, *Small*, 2022, **18**(23), 2107575, DOI: 10.1002/smll.202107575.

2 U. Chand, K.-C. Huang, C.-Y. Huang and T.-Y. Tseng, Mechanism of Nonlinear Switching in HfO_2 -Based Crossbar RRAM With Inserting Large Bandgap Tunneling Barrier Layer, *IEEE Trans. Electron Devices*, 2015, **62**(11), 3665–3670, DOI: 10.1109/TED.2015.2471835.

3 B. J. Choi, D. S. Jeong, S. K. Kim, C. Rohde, S. Choi, J. H. Oh, H. J. Kim, C. S. Hwang, K. Szot, R. Waser, B. Reichenberg and S. Tiedke, Resistive Switching Mechanism of TiO_2 Thin Films Grown by Atomic-Layer Deposition, *J. Appl. Phys.*, 2005, **98**(3), 033715, DOI: 10.1063/1.2001146.

4 G. González-Cordero, M. B. González, H. García, F. Campabadal, S. Dueñas, H. Castán, F. Jiménez-Molinos and J. B. Roldán, A Physically Based Model for Resistive Memories Including a Detailed Temperature and Variability Description, *Microelectron. Eng.*, 2017, **178**, 26–29, DOI: 10.1016/j.mee.2017.04.019.

5 F. Zahoor, T. Z. Azni Zulkifli and F. A. Khanday, Resistive Random Access Memory (RRAM): An Overview of Materials, Switching Mechanism, Performance, Multilevel Cell (Mlc) Storage, Modeling, and Applications, *Nanoscale Res. Lett.*, 2020, **15**(1), 90, DOI: 10.1186/s11671-020-03299-9.

6 T. Boynazarov, J. Lee, H. Lee, S. Lee, H. Chung, D. H. Ryu, H. Abbas and T. Choi, Enhanced Synaptic Properties in HfO_2-Based Trilayer Memristor by Using ZrO_2- Oxygen Vacancy Reservoir Layer for Neuromorphic Computing, *J. Mater. Sci. Technol.*, 2025, **227**, 164–173, DOI: 10.1016/j.jmst.2024.12.020.

7 P. Chi, S. Li, C. Xu, T. Zhang, J. Zhao, Y. Liu, Y. Wang and Y. Xie, PRIME: A Novel Processing-in-Memory Architecture for Neural Network Computation in ReRAM-Based Main Memory. In 2016 ACM/IEEE 43rd Annual International Symposium on Computer Architecture (ISCA), IEEE: Seoul, South Korea, 2016, pp 27–39, DOI: 10.1109/ISCA.2016.13.

8 M. Ismail, U. Chand, C. Mahata, J. Nebhen and S. Kim, Demonstration of Synaptic and Resistive Switching Characteristics in $W/TiO_2/HfO_2/TaN$ Memristor Crossbar Array for Bioinspired Neuromorphic Computing, *J. Mater. Sci. Technol.*, 2022, **96**, 94–102, DOI: 10.1016/j.jmst.2021.04.025.

9 G. S. Kim, H. Song, Y. K. Lee, J. H. Kim, W. Kim, T. H. Park, H. J. Kim, K. M. Kim and C. S. Hwang, Defect-Engineered Electroforming-Free Analog HfO_x Memristor and Its Application to the Neural Network, *ACS Appl. Mater. Interfaces*, 2019, **11**(50), 47063–47072, DOI: 10.1021/acsami.9b16499.

10 G. Kim, D. Yoo, H. So, S. Park, S. Kim, M.-J. Choi and S. Kim, Precise Weight Tuning in Quantum Dot-Based Resistive-Switching Memory for Neuromorphic Systems, *Mater. Horiz.*, 2025, **12**(3), 915–925, DOI: 10.1039/D4MH01182A.

11 B. Ku, Y. Abbas, S. Kim, A. S. Sokolov, Y.-R. Jeon and C. Choi, Improved Resistive Switching and Synaptic Characteristics Using Ar Plasma Irradiation on the Ti/HfO_2 Interface, *J. Alloys Compd.*, 2019, **797**, 277–283, DOI: 10.1016/j.jallcom.2019.05.114.

12 B. Li, Y. Wang and Y. Chen, HitM: High-Throughput ReRAM-Based PIM for Multi-Modal Neural Networks. In *Proceedings of the 39th International Conference on Computer-Aided Design*, ACM: Virtual Event USA, 2020, pp 1–7, DOI: 10.1145/3400302.3415663.

13 F. Liu, W. Zhao, Y. Chen, Z. Wang, Z. He, R. Yang, Q. Tang, T. Yang, C. Zhuo and L. Jiang, PIM-DH: ReRAM-Based Processing-in-Memory Architecture for Deep Hashing Acceleration. In *Proceedings of the 59th ACM/IEEE Design Automation Conference*, ACM: San Francisco California, 2022, pp 1087–1092, DOI: 10.1145/3489517.3530575.

14 D. Maldonado, A. Cantudo, E. Perez, R. Romero-Zaliz, E. Perez-Bosch Quesada, M. K. Mahadevaiah, F. Jimenez-Molinos, C. Wenger and J. B. Roldan, $TiN/Ti/HfO_2/TiN$ Memristive Devices for Neuromorphic Computing: From Synaptic Plasticity to Stochastic Resonance, *Front. Neurosci.*, 2023, **17**, 1271956, DOI: 10.3389/fnins.2023.1271956.

15 J. Wang, X. Zhuge and F. Zhuge, Hybrid Oxide Brain-Inspired Neuromorphic Devices for Hardware Implementation of Artificial Intelligence, *Sci. Technol. Adv. Mater.*, 2021, **22**(1), 326–344, DOI: 10.1080/14686996.2021.1911277.

16 H. García, G. Vinuesa, T. D. Val, K. Kalam, M. B. González, F. Campabadal, S. Dueñas and H. Castán, Multilevel Conductance Modulation in HfO_2, Al_2O_3, and HfO_2/Al_2O_3 Bilayer Memristors, *Solid-State Electron.*, 2026, **231**, 109294, DOI: 10.1016/j.sse.2025.109294.

17 G. Vinuesa, O. G. Ossorio, H. García, B. Sahelices, H. Castán, S. Dueñas, M. Kull, A. Tarre, T. Jõgiaas, A. Tamm, A. Kasikov and K. Kukli, Effective Control of Filament Efficiency by Means of Spacer $HfAlO_x$ Layers and Growth Temperature in HfO_2 Based ReRAM Devices, *Solid-State Electron.*, 2021, **183**, 108085, DOI: 10.1016/j.sse.2021.108085.

18 Y.-C. Chen, H.-C. Yu, C.-Y. Huang, W.-L. Chung, S.-L. Wu and Y.-K. Su, Nonvolatile Bio-Memristor Fabricated with Egg Albumen Film, *Sci. Rep.*, 2015, **5**(1), 10022, DOI: 10.1038/srep10022.

19 M. K. Hota, M. K. Bera, B. Kundu, S. C. Kundu and C. K. Maiti, A Natural Silk Fibroin Protein-Based Transparent Bio-Memristor, *Adv. Funct. Mater.*, 2012, **22**(21), 4493–4499, DOI: 10.1002/adfm.201200073.

20 K. Krishnan, M. Aono, K. Terabe and T. Tsuruoka, Significant Roles of the Polymer Matrix in the Resistive Switching

Behavior of Polymer-Based Atomic Switches, *J. Phys. Appl. Phys.*, 2019, **52**(44), 445301, DOI: 10.1088/1361-6463/ab35bf.

21 T. Dehury, S. Kumar, A. S. Kumar Sinha, M. Gupta and C. Rath, Thickness Dependent Phase Transformation and Resistive Switching Performance of HfO_2 Thin Films, *Mater. Chem. Phys.*, 2024, **315**, 129035, DOI: 10.1016/j.matchemphys.2024.129035.

22 K. Kukli, L. Aarik, G. Vinuesa, S. Dueñas, H. Castán, H. García, A. Kasikov, P. Ritslaid, H.-M. Piirsoo and J. Aarik, Structure and Electrical Behavior of Hafnium-Praseodymium Oxide Thin Films Grown by Atomic Layer Deposition, *Materials*, 2022, **15**(3), 877, DOI: 10.3390/ma15030877.

23 A. Napolean, N. Sivamangai, S. Rajesh, R. NaveenKumar, N. Nithya, S. Kamalnath and N. Aswathy, Review on Role of Nanoscale HfO_2 Switching Material in Resistive Random Access Memory Device, *Emergent Mater.*, 2022, **5**(2), 489–508, DOI: 10.1007/s42247-022-00356-0.

24 J. Pan, H. He, Q. Huang, Y. Gao, Y. Lin, R. He and H. Chen, HfO_2-Based Resistive Random Access Memory with an Ultrahigh Switching Ratio, *J. Appl. Phys.*, 2024, **136**(7), 075701, DOI: 10.1063/5.0213173.

25 S. W. Ryu, S. Cho, J. Park, J. Kwac, H. J. Kim and Y. Nishi, Effects of ZrO_2 Doping on HfO_2 Resistive Switching Memory Characteristics, *Appl. Phys. Lett.*, 2014, **105**(7), 072102, DOI: 10.1063/1.4893568.

26 D. H. Shin, H. Park, N. Ghenzi, Y. R. Kim, S. Cheong, S. K. Shim, S. Yim, T. W. Park, H. Song, J. K. Lee, B. S. Kim, T. Park and C. S. Hwang, Multiphase Reset Induced Reliable Dual-Mode Resistance Switching of the Ta/HfO_2/RuO_2 Memristor, *ACS Appl. Mater. Interfaces*, 2024, **16**(13), 16462–16473, DOI: 10.1021/acsami.3c19523.

27 A. S. Sokolov, Y.-R. Jeon, S. Kim, B. Ku, D. Lim, H. Han, M. G. Chae, J. Lee, B. G. Ha and C. Choi, Influence of Oxygen Vacancies in ALD HfO_{2-x} Thin Films on Non-Volatile Resistive Switching Phenomena with a Ti/HfO_{2-x}/Pt Structure, *Appl. Surf. Sci.*, 2018, **434**, 822–830, DOI: 10.1016/j.apsusc.2017.11.016.

28 Y. Wang, Q. Liu, S. Long, W. Wang, Q. Wang, M. Zhang, S. Zhang, Y. Li, Q. Zuo, J. Yang and M. Liu, Investigation of Resistive Switching in Cu-Doped HfO_2 Thin Film for Multilevel Non-Volatile Memory Applications, *Nanotechnology*, 2010, **21**(4), 045202, DOI: 10.1088/0957-4484/21/4/045202.

29 Q. Wang, G. Niu, S. Roy, Y. Wang, Y. Zhang, H. Wu, S. Zhai, W. Bai, P. Shi, S. Song, Z. Song, Y.-H. Xie, Z.-G. Ye, C. Wenger, X. Meng and W. Ren, Interface-Engineered Reliable HfO_2 -Based RRAM for Synaptic Simulation, *J. Mater. Chem. C*, 2019, 7(40), 12682–12687, DOI: 10.1039/C9TC04880D.

30 Z. Yong, K.-M. Persson, M. Saketh Ram, G. D'Acunto, Y. Liu, S. Benter, J. Pan, Z. Li, M. Borg, A. Mikkelsen, L.-E. Wernersson and R. Timm, Tuning Oxygen Vacancies and Resistive Switching Properties in Ultra-Thin HfO_2 RRAM via TiN Bottom Electrode and Interface Engineering, *Appl. Surf. Sci.*, 2021, **551**, 149386, DOI: 10.1016/j.apsusc.2021.149386.

31 A. Zeinati, D. Misra, D. H. Triyoso, S. Shrestha, K. Tapily, R. D. Clark, S. Consiglio, C. S. Wajda and G. J. Leusink, Process Optimization for Low Power HfO_2 -Based Resistive Switching Devices for In-Memory Computing Application, *ECS J. Solid State Sci. Technol.*, 2025, **14**(6), 063007, DOI: 10.1149/2162-8777/ade3a3.

32 C. Hu, M. D. McDaniel, A. Posadas, A. A. Demkov, J. G. Ekerdt and E. T. Yu, Highly Controllable and Stable Quantized Conductance and Resistive Switching Mechanism in Single-Crystal TiO_2 Resistive Memory on Silicon, *Nano Lett.*, 2014, **14**(8), 4360–4367, DOI: 10.1021/nl501249q.

33 S. K. Kim, B. J. Choi, K. J. Yoon, Y. W. Yoo and C. S. Hwang, Control of Conducting Filaments in TiO_2 Films by a Thin Interfacial Conducting Oxide Layer at the Cathode, *Appl. Phys. Lett.*, 2013, **102**(8), 082903, DOI: 10.1063/1.4793577.

34 D.-H. Kwon, K. M. Kim, J. H. Jang, J. M. Jeon, M. H. Lee, G. H. Kim, X.-S. Li, G.-S. Park, B. Lee, S. Han, M. Kim and C. S. Hwang, Atomic Structure of Conducting Nanofilaments in TiO_2 Resistive Switching Memory, *Nat. Nanotechnol.*, 2010, **5**(2), 148–153, DOI: 10.1038/nnano.2009.456.

35 S. C. Oh, H. Y. Jung and H. Lee, Effect of the Top Electrode Materials on the Resistive Switching Characteristics of TiO_2 Thin Film, *J. Appl. Phys.*, 2011, **109**(12), 124511, DOI: 10.1063/1.3596576.

36 K.-L. Lin, T.-H. Hou, J. Shieh, J.-H. Lin, C.-T. Chou and Y.-J. Lee, Electrode Dependence of Filament Formation in HfO_2 Resistive-Switching Memory, *J. Appl. Phys.*, 2011, **109**(8), 084104, DOI: 10.1063/1.3567915.

37 R. Jiang, Z. Han and X. Du, Reliability/Uniformity Improvement Induced by an Ultrathin TiO_2 Insertion in Ti/HfO_2/Pt Resistive Switching Memories, *Microelectron. Reliab.*, 2016, **63**, 37–41, DOI: 10.1016/j.microrel.2016.05.013.

38 J. Park, H. Jang, Y. Byun, H. Na, H. Ji and S. Kim, Improved Memory and Synaptic Device Performance of HfO_2-Based Multilayer Memristor by Inserting Oxygen Gradient TiO_x Layer, *Chaos, Solitons Fractals*, 2025, **191**, 115910, DOI: 10.1016/j.chaos.2024.115910.

39 W. Zhang, J.-Z. Kong, Z.-Y. Cao, A.-D. Li, L.-G. Wang, L. Zhu, X. Li, Y.-Q. Cao and D. Wu, Bipolar Resistive Switching Characteristics of HfO_2/TiO_2/HfO_2 Trilayer-Structure RRAM Devices on Pt and TiN-Coated Substrates Fabricated by Atomic Layer Deposition, *Nanoscale Res. Lett.*, 2017, **12**(1), 393, DOI: 10.1186/s11671-017-2164-z.

40 S. Lee, J. Kim and S. Kim, Self-Aligned TiO_x-Based 3D Vertical Memristor for a High-Density Synaptic Array, *Front. Phys.*, 2024, **19**(6), 63203, DOI: 10.1007/s11467-024-1419-2.

41 F. F. Athena, M. P. West, J. Hah, R. Hanus, S. Graham and E. M. Vogel, Towards a Better Understanding of the Forming and Resistive Switching Behavior of Ti-Doped HfO_x RRAM, *J. Mater. Chem. C*, 2022, **10**(15), 5896–5904, DOI: 10.1039/D1TC04734E.

42 B. Chakrabarti and E. M. Vogel, Effect of Ti Doping and Annealing on Multi-Level Forming-Free Resistive Random Access Memories with Atomic Layer Deposited HfTiOx Nanolaminate, *Microelectron. Eng.*, 2013, **109**, 193–196, DOI: 10.1016/j.mee.2013.03.092.

43 B. Kim, C. Mahata, H. Ryu, M. Ismail, B.-D. Yang and S. Kim, Alloyed High-k-Based Resistive Switching Memory

in Contact Hole Structures, *Coatings*, 2021, **11**(4), 451, DOI: 10.3390/coatings11040451.

44 K. Fröhlich, M. Ťapajna, A. Rosová, E. Dobročka, K. Hušeková, J. Aarik and A. Aidla, Growth of High-Dielectric-Constant TiO_2 Films in Capacitors with RuO_2 Electrodes, *Electrochem. Solid-State Lett.*, 2008, **11**(6), G19, DOI: 10.1149/1.2898184.

45 K. Fröhlich, B. Hudec, J. Aarik, A. Tarre, D. Machajdík, A. Kasikov, K. Hušeková and Š. Gaži, Post-Deposition Processing and Oxygen Content of TiO_2-Based Capacitors, *Microelectron. Eng.*, 2011, **88**(7), 1525–1528, DOI: 10.1016/j.mee.2011.03.129.

46 L. Aarik, T. Arroval, P. Ritslaid, A. Vask, H. Mändar and J. Aarik, Influence of Substrates on Structure Development and Concentration of Residual Impurities in Hafnium–Titanium-Oxide Films Grown by Atomic Layer Deposition, *Cryst. Growth Des.*, 2023, **23**(1), 548–557, DOI: 10.1021/acs.cgd.2c01174.

47 T. Arroval, L. Aarik, R. Rammula, V. Kruusla and J. Aarik, Effect of Substrate-Enhanced and Inhibited Growth on Atomic Layer Deposition and Properties of Aluminum–Titanium Oxide Films, *Thin Solid Films*, 2016, **600**, 119–125, DOI: 10.1016/j.tsf.2016.01.024.

48 K. Fröhlich, J. Aarik, M. Ťapajna, A. Rosová, A. Aidla, E. Dobročka and K. Hušková, Epitaxial Growth of High-κ TiO_2 Rutile Films on RuO_2 Electrodes, *J. Vac. Sci. Technol. B Microelectron. Nanometer Struct. Process. Meas. Phenom.*, 2009, **27**(1), 266–270, DOI: 10.1116/1.3021030.

49 K. Möldre, L. Aarik, H. Mändar, A. Niilisk, R. Rammula, A. Tarre and J. Aarik, Atomic Layer Deposition of Rutile and TiO_2-II from $TiCl_4$ and O_3 on Sapphire: Influence of Substrate Orientation on Thin Film Structure, *J. Cryst. Growth*, 2015, **428**, 86–92, DOI: 10.1016/j.jcrysgro.2015.07.029.

50 A. Baunthiyal, M. Schowalter, M. Williams, J.-O. Krisponeit, T. Mehrtens, A. Karg, A. Rosenauer, M. Eickhoff and J. Falta, Structural Evolution and Nucleation Dynamics of RF Sputtered Ga_2O_3 Films on Ru(0001): The Impact of Deposition Temperature and Ru Surface Morphology, *APL Mater.*, 2025, **13**(4), 041130, DOI: 10.1063/5.0270431.

51 L. Aarik, A. Tarre, H. Mändar, J. Merisalu, J. Lu, L. Hultman and J. Aarik, Structure and Electrical Properties of Ga_2O_3 Thin Films Grown by Atomic Layer Deposition on Ru and TiN Electrodes, *J. Mater. Chem. C*, 2026, **14**(16), 6870–6883, DOI: 10.1039/D5TC04544D.

52 M. Liu, L. D. Zhang, G. He, X. J. Wang and M. Fang, Effect of Ti Incorporation on the Interfacial and Optical Properties of HfTiO Thin Films, *J. Appl. Phys.*, 2010, **108**(2), 024102, DOI: 10.1063/1.3462467.

53 J. Merisalu, T. Arroval, A. Kasikov, J. Kozlova, M. Rähn, P. Ritslaid, J. Aarik, A. Tamm and K. Kukli, Engineering of Atomic Layer Deposition Process for Titanium-Aluminum-Oxide Based Resistively Switching Medium, *Mater. Sci. Eng. B*, 2022, **282**, 115797, DOI: 10.1016/j.mseb.2022.115797.

54 E. Pérez, Ó. González Ossorio, S. Dueñas, H. Castán, H. García and C. Wenger, Programming Pulse Width Assessment for Reliable and Low-Energy Endurance Performance in Al:HfO_2-Based RRAM Arrays, *Electronics*, 2020, **9**(5), 864, DOI: 10.3390/electronics9050864.

55 H. García, G. Vinuesa, E. García-Ochoa, F. L. Aguirre, M. B. González, F. Jiménez-Molinos, F. Campabadal, J. B. Roldán, E. Miranda, S. Dueñas and H. Castán, Effects of the Voltage Ramp Rate on the Conduction Characteristics of HfO_2-Based Resistive Switching Devices, *J. Phys. Appl. Phys.*, 2023, **56**(36), 365108, DOI: 10.1088/1361-6463/acdae0.